
DEEP SPATIOTEMPORAL CLUTTER FILTERING OF TRANSTHORACIC ECHOCARDIOGRAPHIC IMAGES USING A 3D CONVOLUTIONAL AUTO-ENCODER

Mahdi Tabassian¹, Somayeh Akbari. S¹, Sandro Queirós^{2,3}, Jan D'hooge¹

¹Cardiovascular Imaging and Dynamics, Department of Cardiovascular Sciences, KU Leuven, Leuven, Belgium
mahdi.tabassian@gmail.com

²Life and Health Sciences Research Institute (ICVS), School of Medicine, University of Minho, Braga, Portugal

³ICVS/3B's - PT Government Associate Laboratory, Braga/Guimarães, Portugal

ABSTRACT

This study presents a deep convolutional auto-encoder network for filtering reverberation artifacts, from transthoracic echocardiographic (TTE) image sequences. Given the spatiotemporal nature of these artifacts, the filtering network was built using 3D convolutional layers to suppress the clutter patterns throughout the cardiac cycle. The network was designed by taking advantage of: i) an attention mechanism to focus primarily on cluttered regions and ii) residual learning to preserve fine structures of the image frames. To train the deep network, a diverse set of artifact patterns was simulated and the simulated patterns were superimposed onto artifact-free ultra-realistic synthetic TTE sequences of six ultrasound vendors to generate input of the filtering network. The artifact-free sequences served as ground-truth. Performance of the filtering network was evaluated using unseen synthetic as well as in-vivo artifactual sequences. Satisfactory results obtained using the latter dataset confirmed the good generalization performance of the proposed network which was trained using the synthetic sequences and simulated artifact patterns. Suitability of the clutter-filtered sequences for further processing was assessed by computing segmental strain curves from them. The results showed that the large discrepancy between the strain profiles computed from the cluttered segments and their corresponding segments in the clutter-free images was significantly reduced after filtering the sequences using the proposed network. The trained deep network could process an artifactual TTE sequence in a fraction of a second and can be used for real-time clutter filtering. Moreover, it can improve the precision of the clinical indexes that are computed from the TTE sequences. The source code of the proposed method is available at: <https://github.com/MahdiTabassian/Deep-Clutter-Filtering/tree/main>.

Keywords Spatiotemporal clutter filtering · 3D convolutional auto-encoder · attention · transthoracic echocardiography · residual learning

1 Introduction

Transthoracic echocardiography (TTE) has become the primary noninvasive imaging modality to quantify myocardial morphology and function in order to diagnose cardiovascular diseases. However, accuracy of visual readings of the cardiologists as well as performance of algorithms designed to measure cardiac characteristics (e.g. a segmentation or a speckle-tracking algorithm), and as a consequence the diagnostic value of the TTE, can significantly be degraded by the presence of acoustic clutter and more specifically the reverberation artifact that is a prevalent type of clutter in the ultrasound images. Patterns of this type of clutter are spatiotemporally variable given that they are mainly generated by some of the slow-moving organs like the ribs and lungs.

The classic approach for clutter filtering is linear decomposition of the acquired ultrasound images into clutter and signal of interest components using a set of bases or kernels. The bases that correspond to the clutter components or

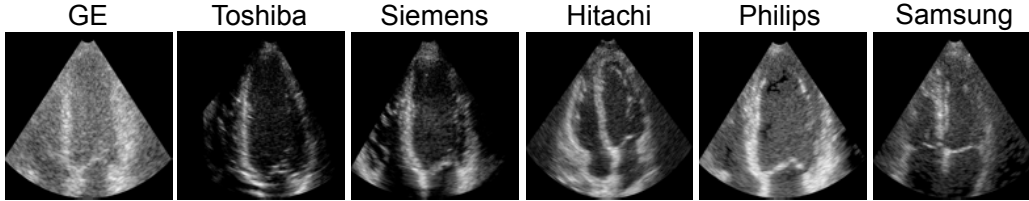


Figure 1: Examples of the ultra-realistic synthetic images of six ultrasound vendors ([15]).

the data reconstructed with the clutter bases are then left out in order to obtain the clutter-filtered ultrasound images. Signal and clutter bases can be defined a priori or can be learned from the data. The discrete Fourier transform [1] and the wavelet transform [2] are examples of the clutter filtering methods that use pre-defined bases. Singular value decomposition (SVD) is the most widely used approach to learn bases for clutter filtering [3, 4] but other dictionary learning techniques like K-SVD [5] and morphological component analysis [6] have also been used for this purpose.

Compared to the approaches that use pre-defined bases for clutter rejection, the learning strategies have the advantage of adapting their bases to the data characteristics enabling them to better filter clutter artifacts. Nonetheless, the learning strategies that are used in the SVD-based filtering methods have some limitations that hamper their efficient operation including: i) linear data modeling, ii) lack of hierarchical representation of the data, iii) usage of a relatively small set of bases for decomposing the data, and iv) regional filtering. In addition to these limitations, defining a proper threshold for finding the clutter bases is a challenge that should be met when a classic clutter filtering method is used.

The mentioned constraints can be circumvented by using a deep convolutional neural network (CNN) that provides hierarchical representation of the data based on a non-linear combination of a lot of bases/kernels while taking global characteristics of the data into account. Such a network also eliminates the need for identifying the clutter bases for filtering a given artifactual image as it adaptively gives higher weights to the bases that best model the clutter patterns present in the image.

As such, CNNs have recently been used in several studies as sophisticated image processing tools to enhance the quality of ultrasound images. In [7, 8, 9], 2D CNNs have been employed in the structure of a generative adversarial network for despeckling of ultrasound images and enhancing their contrast. 2D CNNs were used in [10] to learn a mapping between low- and high-quality subspaces of the radiofrequency images to enhance the quality of images reconstructed from a single plane wave transmission acquisition scheme. A 3D CNN architecture was trained in [11] to remove reverberation and thermal noise from raw ultrasound channel data. A 2D deep auto-encoder network was used in [12] for denoising and acoustic shadowing removal in 2D TTE images. A 3D (2D + time) convolutional network was presented in [13] to remove superimposed synthetic reverberation clutter patterns from TTE images. In a recent study [14], the authors used the idea of superimposing clutter patterns onto TTE images to teach a 3D convolutional network how to remove haze from in-vivo sequences.

1.1 Statement of contribution

Deep spatiotemporal clutter filtering: Inspired by the promising performance of the CNNs in improving the quality of the ultrasound images, a 3D convolutional auto-encoder network is presented in the current study - to the best of our knowledge for the first time - for *spatiotemporal clutter filtering* of the 3D TTE B-mode images.

Artifactual TTE data simulation: Next to optimal design of a deep network for spatiotemporal clutter filtering, having access to a big dataset which contains a diverse set of artifactual images from different ultrasound machines is essential for training a filtering network which has a high generalization performance and is able to handle various types of the clutter patterns. As such, a large set of different reverberation artifact patterns are simulated for training the deep clutter filtering network in our experiments.

2 Materials and Methods

2.1 Data

In order to learn how to remove clutter from an input TTE sequence, a deep network should be provided with a corresponding clutter-free sequence as its output. It is, thus, important to use output sequences that are completely free of artifacts to make sure that the network learns well how to differentiate clutter from signals of interest. With this in mind, a dataset of ultra-realistic synthetic 2D TTE sequences [15] was used in our experiments. The dataset consisted

of 90 TTE vendor-specific sequences of different ultrasound systems. Each vendor had five different myocardial motion patterns including one normal and four ischemic each imaged at apical two-, three- and four-chamber views. The synthetic myocardial motion patterns of this dataset were obtained through using a complex electromechanical heart model while for computing the realistic vendor-specific speckle texture patterns, real clinical TTE recordings were used. The synthetic 2D images (i.e. frames) of six vendors of this dataset were resized to (128×128) and 50 frames were used to form 2D TTE sequences of size $(128 \times 128 \times 50)$. Figure 1 shows examples of apical four-chamber view images of the normal subject taken from the six vendors in the dataset. It can be seen that the left and right heart chambers have different appearances in the images of the six vendors. This characteristic of the employed synthetic dataset is favorable for training a deep clutter filtering network as it enables the network to learn how to filter artifacts from a variety of the TTE images.

2.2 Clutter simulation

Two common reverberation patterns were simulated in our experiments: i) near-field (NF) and, ii) ribs- and/or lung-induced (RL) clutter. The NF clutter is usually generated by thick layers of fat and intercostal muscle under the skin that reflect the ultrasound beam multiple times before reaching the heart [16]. Because the structures that generate the NF clutter are stationary, this type of clutter has no or very limited movement throughout the cardiac cycle. The second type of clutter patterns are generated when the heart is partially covered by the lung tissue and/or when part of the ultrasound beam is blocked by the ribs. This type of clutter can be static or slowly moving during the cardiac cycle because of the respiration. The interested reader is referred to [16] for further details about the main scenarios that could lead to the simulated clutter patterns.

Given that reverberations can have various patterns and appearances depending on the patient’s physical characteristics, e.g. body-mass index or positions of the ribs and lung tissue, a simulated clutter dataset should contain diverse clutter examples in order to account for the different scenarios that are encountered in practice. Therefore, various NF and RL clutter patterns as well as combinations of the two patterns were simulated in our experiments with the aim of training an efficient deep clutter filtering algorithm that has a high generalization performance.

Both the NF and RL clutter patterns were simulated using the Gaussian distribution given the suitability of this distribution in representing the common clutter patterns that exist in the TTE images. More specifically, brightness changes inside clutter zone and variations in the clutter shape can properly be simulated by means of a bivariate, i.e. 2D, Gaussian distribution for modeling the variations of the clutter patterns in the lateral (i.e. horizontal) and axial (i.e. vertical) directions in a 2D B-mode image. Figure 2 shows how the brightness levels of the clutter pixels can be determined depending on their positions in a rectangular clutter zone. The length and width of the rectangle were selected such that they covered 3σ of the Gaussian distribution values which account for 99.73% of the data that can be taken from this distribution. The grayscale of a pixel j in Figure 2 was determined by first multiplying its horizontal and vertical probability values and then multiplying the obtained probability value with a constant grayscale G . As such, the central pixel i had the largest grayscale value because its probability values were taken from the centers of the two distributions. For other pixels in the clutter zone, the farther they were from the central pixel and the closer to the edges of the rectangle, the lower their probability and as a result their grayscale values were. By using different horizontal and vertical σ s, clutter patterns with various sizes and shapes were generated. Also, a range of G s were used in order to simulate different brightness levels.

2.2.1 NF clutter simulation

The NF clutter data were simulated by taking the following main properties of this type of the clutter into account: i) a larger extension in the axial than the lateral direction, ii) high brightness in the near-field area and above the apex of the heart; and iii) being static, i.e. temporally invariant. Table 1 lists three vertical sigmas (σ_v), two horizontal sigmas (σ_h) and three grayscale values that were used for simulating the NF clutter patterns. Using all combinations of these parameters, 18 distinct NF clutter patterns were simulated. The center of the clutter zone was placed above the apex of the heart but its position in the axial direction was selected randomly. Because the NF clutter was considered to be static, the position of a simulated pattern was the same in all 50 frames of a B-mode sequence. Figure 3(a) shows an example of a generated clutter pattern with $\sigma_v = 20$, $\sigma_h = 10$ and $G = 255$ along with the result of superimposing it onto an apical four-chamber view B-mode image (i.e. adding the clutter pattern to the B-mode image) to have a cluttered image. All the pixels of the clutter zone that were located outside the sector of the B-mode image were pruned by setting them to zero in the cluttered image as to respect the sectorial field-of-view of a cardiac phase array recording.

2.2.2 RL clutter simulation

The main characteristics of the RL clutter considered for simulation were: i) having ellipsoidal shapes with a larger extension in the radial than the lateral direction, ii) being perpendicular to the ultrasound image line and close to

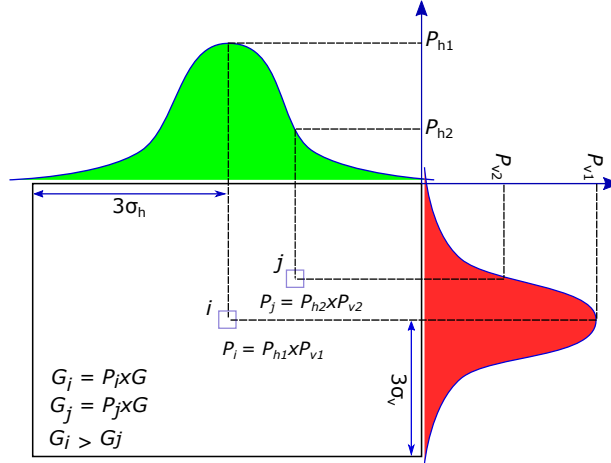


Figure 2: Schematic representation of the approach used for simulating the reverberation patterns. The brightness levels of a clutter pixel is determined depending on its distance from the center of a rectangle whose length and width cover 3σ of 2 different Gaussian distributions. The central pixel i is located in the centers of the distributions and has the highest grayscale value whereas a pixel which is close to the corners of the rectangle corresponds to small probability values, taken from the Gaussian distributions, and has a lower grayscale value than the central pixel.

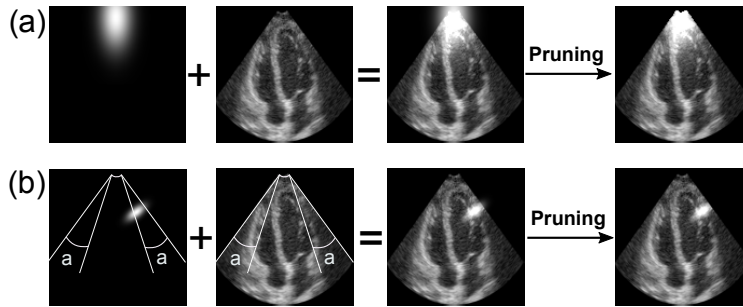


Figure 3: Schematic representation of generating artifactual B-mode images using the simulated (a) NF and (b) RL clutter patterns. The simulated patterns are added to the artifact-free images and the clutter pixels located outside the image sectorial field-of-view were removed. Location of the RL clutter patterns was considered to be within a right and left sub-sector with an opening angle $a = 35^\circ$ to ensure that the simulated patterns are not far away from the sector edges of the B-mode image.

Table 1: Characteristics of the simulated near-field (NF) clutter patterns

σ_v	σ_h	G	No. patterns
[10, 15, 20]	[5, 10]	[150, 200, 255]	18

Table 2: Characteristics of the simulated ribs- and/or lung-induced (RL) clutter patterns

σ_v	σ_h	G	Cardiac level	Sector edge	Velocity (cm/s)	No. patterns
[3, 5]	[7, 9, 11]	[150, 200, 255]	(base, mid, apex)	(right, left)	[0, 0.5, 1]	324

the right or left sectorial borders of the image, iii) being static or slowly moving in the lateral direction during the cardiac cycle. Table 2 shows a list of parameters that was used for simulating 324 distinct RL clutter patterns. After generating a clutter pattern using a combination of σ_v , σ_h and G values, it was rotated around its center such that it was perpendicular to the sector edge. Figure 3(b) demonstrates an example of a simulated RL clutter pattern with $\sigma_v = 5$, $\sigma_h = 9$ and $G = 255$. To ensure that the clutter position was not far from the sectorial borders, a right and a left sub-sector was defined with an opening angle $a = 35^\circ$ and the center of the clutter zone was placed inside either of

Table 3: Characteristics of the simulated NF & RL clutter patterns

NF			RL					
σ_v	σ_h	G	σ_v	σ_h	G	Cardiac level	Sector edge	Velocity (cm/s)
[10, 15, 20]	[5, 10]	[200, 255]	5	[9, 11]	[200, 255]	(mid, apex)	right	[0, 1]
No. patterns:		192						

them. After superimposing the clutter pattern onto the clutter-free image, the obtained cluttered image was pruned to remove clutter pixels located outside the sectorial field-of-view of the image.

As shown in Table 2, the simulated RL clutter included dynamic patterns with two different velocities, 0.5 and 1 cm/s . In our experiments, it was assumed that - as a rough estimate - the average myocardial velocity can be considered to be $\approx 10 cm/s$ [17]. As such, the simulated dynamic RL clutter had 5 or 10% of the average myocardial velocity, representing the slow-moving clutter patterns.

2.2.3 Joint NF and RL clutter simulation

Given that in clinical practice both the NF and RL clutter patterns can exist in a TTE image, the simulated data included combinations of subsets of the patterns listed in Tables 1 and 2. They are 12 NF and 16 RL clutter patterns whose combinations led to 192 distinct clutter patterns as shown in Table 3. Adding these patterns to those of the other two clutter groups resulted in 524 simulated NF and/or RL clutter patterns.

2.3 Deep spatiotemporal clutter filtering network

Motivated by the successful applications of the deep convolutional auto-encoders, and more specifically the 2D U-Net [18], in different ultrasound image enhancement tasks [7, 8, 9, 10, 12], an algorithm was designed based on the 3D U-Net [19] for clutter filtering of the TTE B-mode image sequences in the present study. The rationale behind designing a 3D filtering network was to account for the spatiotemporal nature of the reverberation clutter. This type of artifact affects the 2D B-mode images throughout the cardiac cycle resulting in patterns that slowly move in time.

Using a 3D network, behavior of the clutter patterns can be learned both in space and time and the generated filtered images remain *spatiotemporally coherent*. The architecture of the proposed clutter filtering algorithm is shown in Figure 4. It is designed such that it can satisfy two important requirements: i) *only suppress the cluttered regions in a 3D image* ; and ii) *preserve the characteristics of the clutter-free regions*.

Fulfillment of these requirements is essential to ensure that the cardiac characteristics computed from the filtered images are reliable. For example, it is important that the speckle patterns of the clutter-free regions in the cluttered and clutter-filtered images are the same, or very similar, to make sure that the strain profiles that are computed from these regions before and after clutter filtering using a speckle-tracking algorithm are identical. To address these requirements, the original architecture of the 3D U-Net was adjusted for the clutter filtering task using:

1. an input-output skip connection [20, 21, 10] to train the filtering network based on residual learning [22], and
2. attention gates [23, 24].

As shown in Figure 4, function of the input-output skip connection is adding the input of the U-Net to the output of its last decoding block before generating the final output. Preserving fine structures of the ground-truth image in the image generated by the U-Net, is the main advantage of training the deep network based on residual learning and through using input-output skip connection as demonstrated in the image reconstruction [20, 10] and denoising [21] applications. Using this connection in the architecture of the proposed clutter filtering network thus ensures that fine image structures of the clutter-free regions are preserved in the clutter-filtered images.

The idea of using attention gate (AG) in the architecture of a feed-forward CNN was proposed in [23] where a set of weights were learned to highlight salient regions in the mid-level feature maps by using the contextual information provided by the high-level feature maps. AG was integrated in the U-Net architecture in [24] to find salient regions in the feature maps generated at each level of its encoding path. Experimental results on different medical image segmentation and classification tasks showed performance improvement of the AG U-Net over the vanilla U-Net. By incorporating the AG modules into the architecture of our proposed clutter filtering network, cluttered zones in the learned feature maps can be highlighted as the salient regions. This helps the network to focus on the cluttered regions resulting in efficient suppression and reconstruction of these regions.

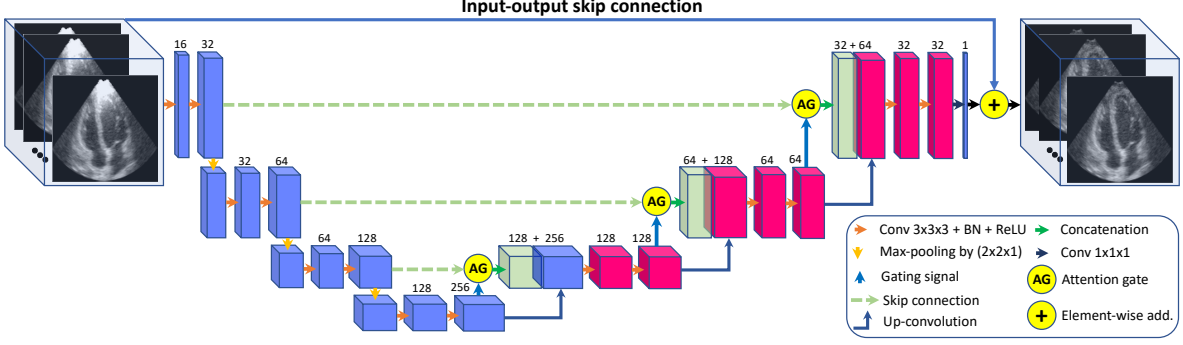


Figure 4: Architecture of the spatiotemporal filtering network. It is a fully convolutional auto-encoder designed based on the 3D U-Net to generate filtered TTE sequences which are coherent both in space and time. An input-output skip connection was added to the auto-encoder for preserving fine image structures, together with the attention gate (AG) modules to aid the network focusing on the clutter zones. Size of the max-pooling window was set to $(2 \times 2 \times 1)$ in order to preserve the original temporal dimension, i.e. the number of frames, of the input TTE sequences.

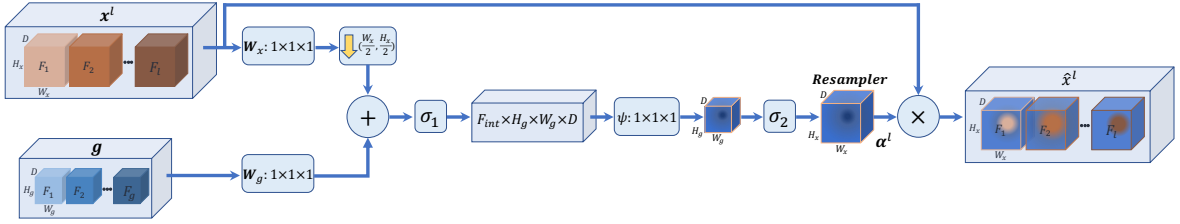


Figure 5: Internal architecture of the additive AG module. The salient regions on the feature maps at scale l , \mathbf{x}^l , are highlighted by taking advantage of the information encoded in the coarse feature maps of the next scale (\mathbf{g}).

2.3.1 AG module in the 3D U-Net architecture

As shown in Figure 4, the AGs are located on the skip connections of the U-Net architecture at different image scales. The AG module at each scale l has two input signals: i) the feature maps \mathbf{x}^l generated in the encoding path, ii) the coarse feature maps $\mathbf{g} \in \mathbb{R}^{F_g}$, also called gating signal, generated in the next scale containing more contextual information than \mathbf{x}^l . Through using the additive attention strategy [25], \mathbf{x}^l and \mathbf{g} are jointly used to highlight salient regions in the computed feature maps at scale l as follows [24]:

$$q_{att,i}^l = \Psi^T(\sigma_1(\mathbf{W}_x^T \mathbf{x}_i^l + \mathbf{W}_g^T \mathbf{g} + \mathbf{b}_{xg})) + b_\psi \quad (1)$$

$$\alpha^l = \sigma_2(q_{att}^l(\mathbf{x}^l, \mathbf{g}; \Theta_{att})) \quad (2)$$

In 1, $q_{att,i}^l$ represents the value of the intermediate attention map F_{int} for pixel i in the considered feature map, \mathbf{x}_i^l is the pixel-wise feature vector of length F_l . $\mathbf{W}_x \in \mathbb{R}^{F_l \times F_{int}}$, $\mathbf{W}_g \in \mathbb{R}^{F_g \times F_{int}}$, $\Psi^T \in \mathbb{R}^{F_{int} \times 1}$ are linear transformations and $b_\psi \in \mathbb{R}$, $\mathbf{b}_{xg} \in \mathbb{R}^{F_{int}}$ are bias terms. They form the set of parameters of the AG module which is shown with Θ_{att} in (2). After combining the information of the input feature map with the gating signal, the result is passed through an element-wise non-linearity function $\sigma_1(\cdot)$. Values of the computed intermediate attention map are then normalized by passing q_{att}^l through $\sigma_2(\cdot)$. In this study, the ReLU and sigmoid activation functions are used as $\sigma_1(\cdot)$ and $\sigma_2(\cdot)$, respectively. As shown in Figure 5, the input feature map \mathbf{x}^l is down-sampled by a factor 2 to have the same spatial resolution as \mathbf{g} to allow merging the two feature maps. The normalized attention map α^l in (2) is therefore up-sampled by a factor of 2 before it is multiplied with \mathbf{x}^l to highlight the salient regions in the input feature map.

Since the proposed filtering network is 3D, the attention maps highlight salient regions on the learned feature maps throughout the cardiac cycle, i.e. *spatiotemporal attention*.

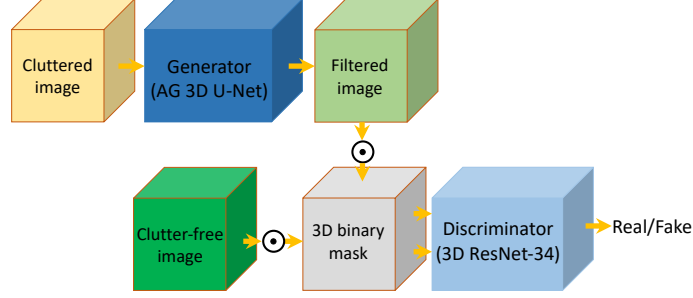


Figure 6: Overview of the employed framework for computing the adversarial loss function. A binary mask was first applied to the cluttered and clutter-filtered images to zero out clutter-free zones in the images. The masked images were then fed into a discriminator network.

2.3.2 Loss function

In addition to the network architecture design, choice of the loss function has a significant impact on the quality of the clutter-filtered images. In this study, three different loss functions were examined for training the proposed deep clutter filtering network.

Reconstruction loss: This loss function measures the mean squared difference between the pixel values of the clutter-free, Y , and clutter-filtered, \hat{Y} , images:

$$L_{rec} = \frac{1}{HWF} \sum_{h=1}^H \sum_{w=1}^W \sum_{f=1}^F (Y_{hwf} - \hat{Y}_{hwf})^2 \quad (3)$$

where F is the number of frames of the TTE sequences and H and W are the height and width of each frame.

Joint reconstruction and adversarial loss: It is known that the reconstruction loss (L_{rec}) tends to generate blurry images when it is used by deep networks for image reconstruction and restoration [26, 27]. An explanation for this phenomenon is that such a network selects an average image sample from the probability distribution of too many possible output images resulting in a blurry reconstructed image [28, 26]. A possible solution for dealing with this problem is adding an adversarial loss to the reconstruction loss as shown in [26, 29]. Using an adversarial loss function enables a deep network to select one of the multiple correct answers instead of considering the average of these answers as the best output [28]. The joint loss function is composed of the reconstruction loss shown in (3) and an adversarial loss computed based on Generative Adversarial Networks (GAN) [30]:

$$L_{rec\&adv} = \lambda_{rec}L_{rec} + \lambda_{adv}L_{adv} \quad (4)$$

where λ_{rec} and λ_{adv} are regularization parameters. The adversarial loss L_{adv} was computed by training the discriminator using a masked version of the clutter-filtered and clutter-free images (see Figure 6):

$$L_{adv} = \max_D \mathbb{E}_{\mathbf{y} \in \mathcal{Y}} [\log(D(\mathbf{y} \odot \mathbf{m})) + \log(1 - D((G(\mathbf{z}) \odot \mathbf{m})))] \quad (5)$$

where G and D represent the generator and the discriminator networks, $G(\mathbf{z})$ is the clutter-filtered image, \mathbf{y} is the clutter-free image, \odot is the element-wise product operation and \mathbf{m} is a 3D binary mask with pixel values equal to 1 for the clutter zones and 0 elsewhere. The reason behind applying a binary mask to the input images was enabling the discriminator to focus on the reconstructed pixels corresponding to the clutter zones to better evaluate the goodness of the generated pixel values for these zones. The AG U-Net with the input-output skip connection (Figure 4) was used as the generator and a 3D ResNet-34 ([22]) was employed as the discriminator.

Joint reconstruction and perceptual loss: An alternative approach for generating realistic filtered images is to use a joint loss function composed of the reconstruction and perceptual losses [31]:

$$L_{rec\&prc} = \lambda_{rec}L_{rec} + \lambda_{prc}L_{prc} \quad (6)$$

where L_{prc} is computed using a pre-trained deep neural network which measures high-level perceptual differences between the pixel values generated by the clutter filtering network and those of the ground-truth. The perceptual

difference is quantified by comparing the activation values, i.e. values of the feature maps, of some of the layers of the pre-trained network for the generated output of the filtered and the ground-truth images.

A vanilla 3D U-Net was trained as an auto-encoder network using the clutter-free TTE images for learning the essential characteristics of these images to reconstruct them accurately. Feature maps of the first and second levels of the encoding path of the network, ReLU1_2 and ReLU2_2, were employed for computing the perceptual loss.

3 Experiments

3.1 Network training

The proposed clutter filtering network was trained using the data of three randomly selected ischemic categories. The training set was composed of 28836 TTE sequences, which is the multiplication of the number of the generated clutter patterns (534, see Section 2.1), views (3), vendors (6) and ischemic groups (3). The data of the fourth ischemic group were used as a validation set to tune the parameters of the network and determine the best set of network’s weights. The sequences of the normal group were used as the test set.

The overall architecture of the 3D clutter filtering network is similar to the 3D U-Net [19] but the two networks have some differences as well. In addition to using an input-output skip connection and the AG modules in the architecture of the proposed network, the number of initial 3D kernels was set to 16 instead of 32 initial kernels used in the 3D U-Net (see Figure 4). This resulted in a relatively light 3D network with almost 5 million (M) trainable parameters, i.e. weights, compared to 19M parameters of the original 3D U-Net. The other difference was the size of the pooling window of the max-pooling layers. To preserve the temporal information of the TTE sequences at the different levels of the encoding path of the 3D filtering network, a pooling window of size $(2 \times 2 \times 1)$ was used in the 3D max-pooling layers at the end of each level. As a result, the input tensors at all levels of the network had a depth equal to 50, i.e. the number of frames, while the width and height of a tensor at level l was half of those of level $l - 1$.

With the aim of training a filtering network that works independent of the starting point of the TTE sequence in the cardiac cycle (e.g. end-systole, end-diastole) and for augmenting the training data, a subset of the input-output training sequences were shifted in time such that the starting frames were taken from different time points during the cardiac cycle. An input-output sequence was selected based on the outcome of the Bernoulli distribution, i.e. 0 or 1, with $p = 0.5$ and its first frame was randomly chosen from $[1, 50]$ range.

The proposed 3D clutter filtering network was trained using the loss functions mentioned in Section 2.3.2, the TensorFlow library, the Adam optimizer with a learning rate of 10^{-4} , 20 epochs and one NVIDIA Tesla P100 GPU.

The validation loss values were monitored during the training phase to find the best model for each of the examined deep filtering networks. Also, the best regularization parameters of the joint loss functions were determined by considering the results obtained on the validation data.

3.2 Benchmark networks

The performance of the proposed 3D clutter filtering network was compared with those of the following benchmark deep networks: i) a 3D U-Net without the input-output skip connection but with the AG modules in its architecture, ii) a 3D U-Net with the input-output skip connection but without the AG modules, iii) a vanilla 3D U-Net without the input-output skip connection and the AG modules [13], and iv) a 2D U-Net with an architecture similar to the proposed network, i.e. with the input-output skip connection and the AG modules.

The 2D filter was considered to investigate the utility of the 3D convolutional kernels for preserving temporal coherence of the TTE sequences during clutter filtering whereas the 3D benchmark networks were used to evaluate the advantage of incorporating the input-output skip connection and the AG modules in the architecture of the 3D filter. The benchmark networks were trained using the reconstruction loss, L_{rec} . Table 4 lists the general characteristics of the benchmark networks as well as the proposed filtering network trained with the different loss functions.

4 Results and Discussion

The best model for each of the deep filters listed in Table 4 was used to evaluate its performance on the unseen test sequences of the normal group. The time required to process a test TTE sequence using the NVIDIA Tesla P100 GPU was a fraction of a second. For instance, the proposed 3D network could filter a given sequence in less than 200 *ms*. The results obtained on the test TTE sequences are presented in the following sections.

Table 4: List of the examined deep clutter filtering networks.

Clutter filtering network	in-out skip	AG	Loss function
3D (proposed)	Yes	Yes	L_{rec}
3D (proposed)	Yes	Yes	$L_{rec&adv}$
3D (proposed)	Yes	Yes	$L_{rec&prc}$
3D (benchmark net. 1)	No	Yes	L_{rec}
3D (benchmark net. 2)	Yes	No	L_{rec}
3D (benchmark net. 3)	No	No	L_{rec}
2D (benchmark net. 4)	Yes	Yes	L_{rec}

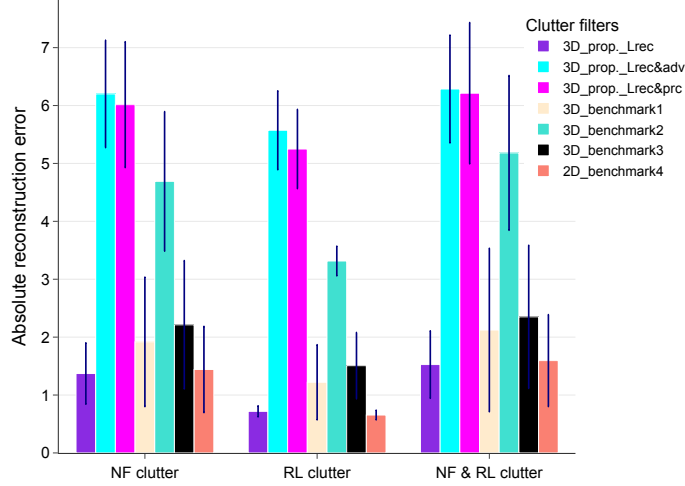


Figure 7: Mean \pm STD of the individual MARE values computed using the clutter-free and clutter-filtered TTE sequences for the 3 categories of the simulated artifacts obtained with the examined filters.

4.1 Overall performance analysis

Performance of the proposed and benchmark clutter filtering networks were compared in terms of mean absolute reconstruction error (MARE) computed using the pixel values of the clutter-filtered and clutter-free testing sequences after scaling their pixels to the range $[0, 255]$.

Figure 7 illustrates mean \pm standard deviation (STD) rates computed from the MARE values of the individual TTE sequences for the three classes of the simulated artifact patterns. For each of the examined networks, the lowest and highest error rates were obtained on the samples of the RL clutter class and the RL & NF clutter class, respectively. This was expected given that the RL clutter patterns had the smallest size among the simulated clutter classes while the patterns of the RF & NF classes contaminated the images the most.

The proposed 3D clutter filtering network trained using the reconstruction loss (L_{rec}), yielded the lowest MARE values as compared to the other 3D networks. The second lowest MARE values among the 3D networks were obtained using the *benchmark network 1*. Both networks were trained using the same loss function and took advantage of the AG modules. However, the benchmark network did not have the input-output skip connection in its architecture which resulted in higher MARE values. Adding the input-output skip connection to the U-Net architecture alone and not incorporating the AG modules, i.e. the *benchmark network 2*, did not help filtering the clutter patterns.

Combination of the input-output skip connection and the AG modules also led to an efficient filtering performance when incorporated into the 2D U-Net, i.e. the *benchmark network 4*. The MARE values obtained using the 2D network are comparable with those of the proposed 3D network (L_{rec}) for the three categories of the simulated clutter patterns (see Figure 7). The MAREs of the 3D network are slightly lower than the 2D network for the NF and NF & RL categories (p -value ≤ 0.01), as the most challenging clutter classes, but it yielded a little higher MARE values for the RL clutter class than the 2D network (p -value ≤ 0.01). However, as it will be shown in the following sections, the proposed 3D network outperformed the 2D network in terms of coherence of the filtered frames and accuracy of the strain curves computed from the filtered frames.

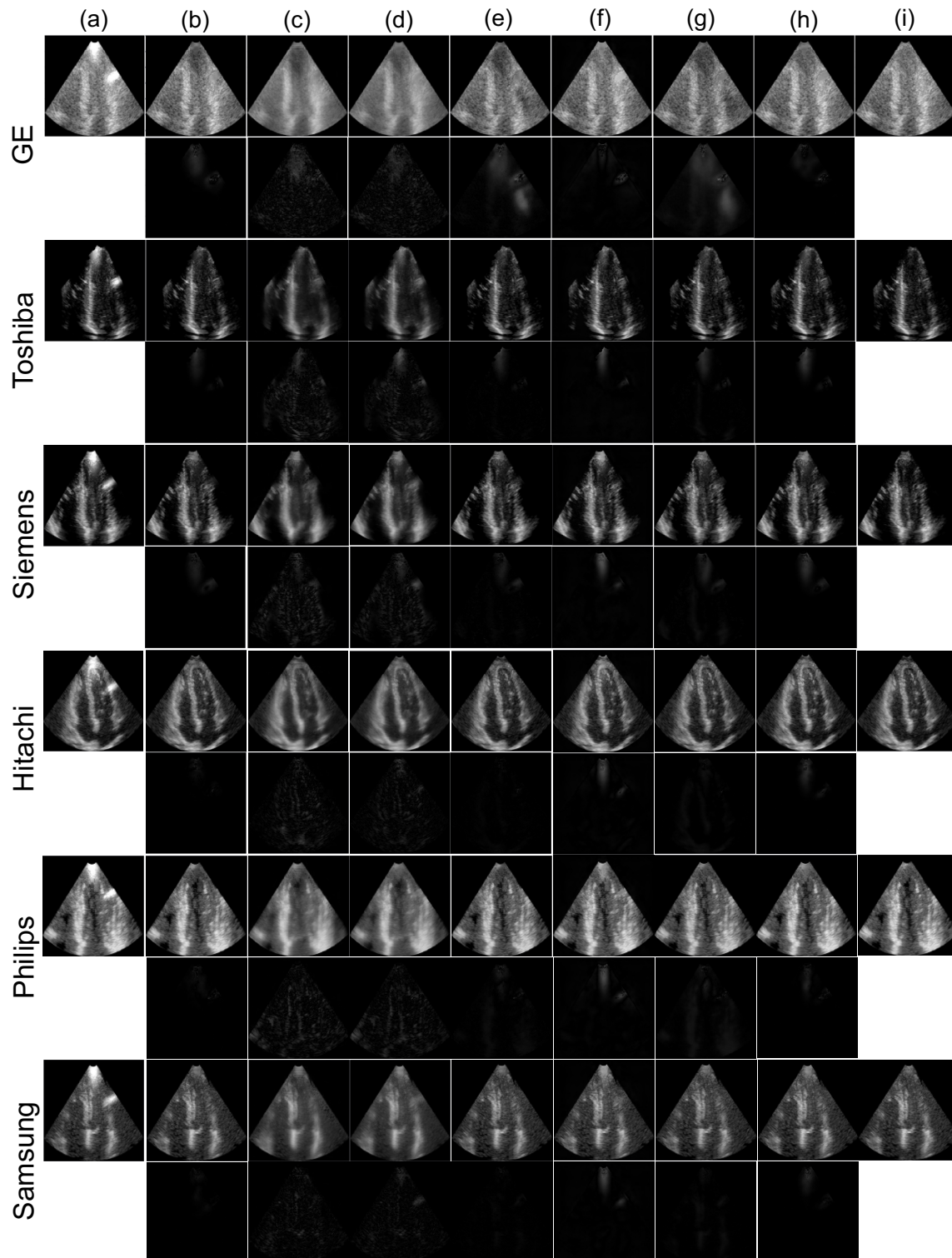


Figure 8: (a) Examples of the cluttered test frames and ((b)-(h)) the clutter-filtered frames of the six vendors generated by the examined deep networks. (b), (c) and (d) The proposed 3D filter trained with L_{rec} , $L_{rec\&adv}$ and $L_{rec\&prc}$, respectively. (e), (f) and (g), the 3D benchmark networks 1-3. (h) the 2D benchmark network. (i) The clutter-free frames. For each vendor, absolute difference images computed from the clutter-filtered and clutter-free frames are shown in the row below the respective filtered frames.

Training the proposed 3D network using the joint loss functions resulted in poor filtering outcomes and much larger MARE than the 3D network trained using L_{rec} only.

To qualitatively evaluate the goodness of the filtering results, examples of the clutter-filtered test images generated by the examined deep networks are shown in Figure 8. For one of the NF & RL clutter patterns [NF ($\sigma_v = 15, \sigma_h = 5, G = 200$); RL ($\sigma_v = 5, \sigma_h = 11, G = 200$)] (see Table 3), the filtering results are demonstrated for each of the six vendors and the middle frames. This figure also shows the absolute difference between each clutter-filtered frame and its corresponding clutter-free frame (column (i)) in the rows below the filtered frames to facilitate assessment of the filtering quality. In line with the quantitative results shown in Figure 7, the best filtered frames for all vendors were generated using the 3D and 2D networks that had input-output skip connection and the AGs in their architectures and were trained using the L_{rec} loss (Figure 8(b) and (h)). For these filters, pixel values of the clutter-free zones are (almost) equal to zero in the absolute difference images and the zones with non-zero, yet very small, pixel values correspond to the cluttered regions. These results suggest that: i) the characteristics of the clutter-free zones are identical in the cluttered and clutter-filtered images; and ii) the filtering networks mainly focused on suppressing the clutter patterns. Therefore, the important requirements that were considered when designing the proposed filtering network (see Section 2.3) were fulfilled.

For the proposed 3D filter trained using the joint loss functions (Figure 8(c) and (d)), the absolute difference images show why the computed MARE values are large (see Figure 7). In these images, the clutter-free zones have non-zero values implying that the filter changed the characteristics of these zones. More specifically, the filters generated smoothed versions of the clutter-free images. For the joint reconstruction and perceptual loss, the filtered frames also have grid-like artifacts (Figure 8 (d)) which are usually present in the output images of a network trained using the perceptual loss function [31]. The smoothness of the filtered frames generated using the joint reconstruction and adversarial loss might be explained by the instability of the training process of GANs [28, 32]. Even though the use of the adversarial loss function led to less blurry filtered pixels for the cluttered zones compared to the results obtained using the pure reconstruction loss, e.g. the NF filtered zones for GE, Siemens and Philips in Figure 8, the clutter-free zones of the filtered and ground-truth frames are different. Also, the generated patterns for the pixels of the cluttered zones do not represent the speckle patterns on the clutter-free images well.

The interested reader is referred to the GitHub repository of the current study to review example video files of the clutter-filtered cine-loops generated by the proposed 3D filter (Figure 8(a)) and the 2D filter (Figure 8(h)) for the six vendors.

4.2 Attention maps analysis

Since the efficient performance of the proposed 3D filtering network highly depends on the role played by the AGs, it is important to analyse the learned attention maps in order to gain more insights into the AG function in the filtering network.

One clutter pattern from each of the three simulated classes was selected and for the middle frame of three vendors, the attention maps learned at the three scales of the 3D U-Net algorithm are demonstrated in Figure 9. This figure shows that the attention maps of the first and third scales ((b) and (d)) highlighted the clutter zones on the feature maps whereas the clutter-free zones and the regions around the clutter patterns, were highlighted on the attention maps of the second scale ((c)). It is, thus, reasonable to conclude that the attention maps of the three scales complement each other and highlight salient regions on the learned feature maps.

As mentioned in Section 2.3.1, the AGs employed by the 3D U-Net generate spatiotemporal attention maps (see Figure 5). To examine the goodness of the generated attention maps in highlighting the clutter zones corresponding to the moving artifacts on the feature maps, examples of the generated attention maps for two different moving artifact patterns are illustrated in Figure 10. The attention maps are superimposed onto the first and last frames of the cluttered TTE sequences to check if the AG module could attend to the moving RL patterns in time. The white arrows are added to Frame 50 to show the positions of the RL patterns on Frame 1. Although positions of the RL patterns changed from Frame 1 to Frame 50, the AG module managed to follow the patterns in time and highlight the clutter zones.

4.3 Coherence analysis

As stated in Section 2.3, generating clutter-filtered TTE sequences which are coherent both in space and time was the main reason behind using a 3D deep network in our study. To quantitatively measure the coherence of a cluttered sequence filtered by the examined deep networks, a new sequence Z was created for each of the filters by computing the absolute difference between the testing clutter-free (Y) and clutter-filtered (\hat{Y}) sequences,

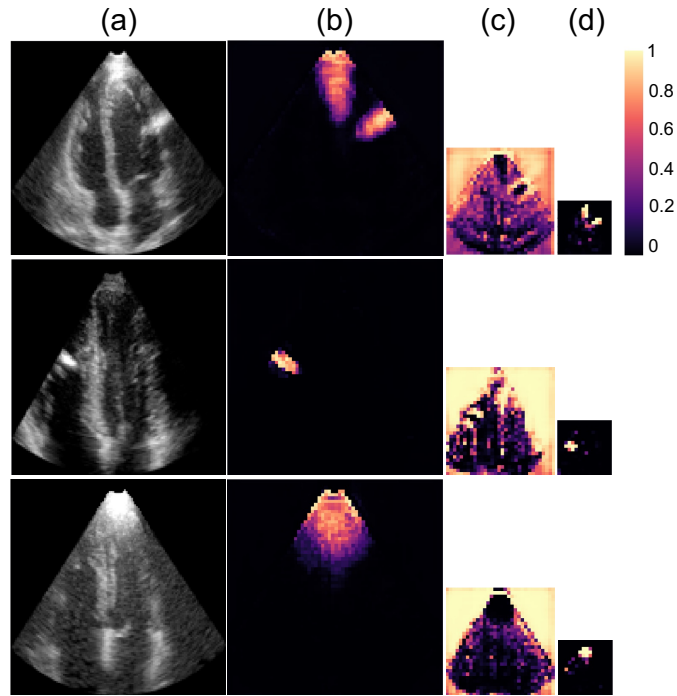


Figure 9: Examples of the generated attention maps for three different clutter patterns and vendors. (a) The cluttered frames, (b) attention maps of the first scale, (c) second scale and (d) third scale of the 3D U-Net. The generated attention maps of the first and third scales highlight the clutter zones on the feature maps while the attention map of the second scale guides the filtering network to focus on regions around the clutter patterns. The color bar on the right shows the range of the normalized attention values.

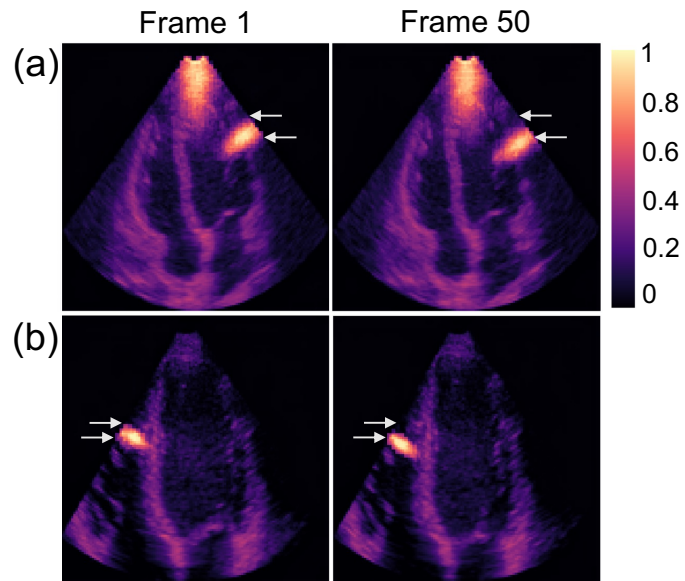


Figure 10: Examples of the generated attention maps for two different moving artifact patterns located on the (a) right and (b) left sectorial border of the TTE sequences of two different vendors. The generated attention maps at scale 1 were superimposed onto the first and last frames of the TTE sequences. Positions of the moving RL clutter patterns on Frame 1 are shown with white arrows on Frame 50 to help estimating the displacements of the patterns throughout the cardiac cycle. These example show that the spatiotemporal AG module could properly follow and highlight the moving clutter patterns.

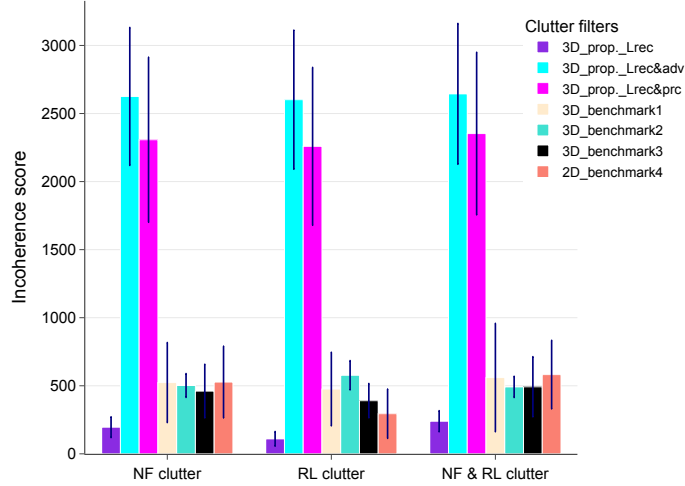


Figure 11: The incoherence scores (Mean±STD) of the deep clutter filtering networks for each of the three categories of the simulated artifact patterns.

$$Z = |Y - \hat{Y}|. \quad (7)$$

The mean absolute difference between the pixel values of the consecutive frames of Z was then computed as:

$$C = \frac{1}{F-1} \sum_{f=2}^F |Z_f - Z_{f-1}| \quad (8)$$

where Z_f is sum of pixel values of frame f . C can be considered as a score that shows how (in)coherent the filtered frames are. A large C indicates that the pixel values in the consecutive filtered frames vary significantly. A small C , on the other hand, shows that the changes in the pixel values in the consecutive frames of Z are negligible implying that the filtered frames are coherent throughout the cardiac cycle.

As an alternative, the coherence score can be directly computed using the clutter-filtered sequences (\hat{Y}). Considering \hat{Y} instead of Z , however, has a major drawback: the computed score is a holistic one which represents the (in)coherence of the entire 2D frames and not the clutter-filtered zones. This score, thus, might fail to properly represent the (in)coherence of the filtered sequences for small clutter patterns.

Figure 11 demonstrates the computed incoherence scores of the examined deep filtering networks for each category of the simulated clutter patterns. The smallest C values belong to the proposed 3D filtering network trained with L_{rec} . These values are significantly smaller than those of the 2D benchmark network ($p < 0.001$). The largest incoherence scores were obtained for the images with the NF & RL clutter patterns. This was expected given that this clutter class contaminated the images more than the two other categories of the simulated clutters. For this clutter class the 3D filters, except for the proposed filter trained with the $L_{rec&adv}$ and $L_{rec&prc}$, produced more coherent filtered frames as compared to the 2D filter. This confirms the advantage of the 3D convolutional layers over their 2D counterparts for modeling temporal evolution of the TTE sequences and filtering the cluttered frames.

The example video files provided in the GitHub repository include Z cine-loops of the proposed 3D filter and the 2D filter. They demonstrate that the TTE sequences filtered by the proposed 3D network are indeed more coherent in space and time and unlike the 2D network, their consecutive frames have very small variations.

4.4 Strain analysis

To evaluate the goodness of the filtering results for further spatiotemporal analyses, the Medical Image Tracking Toolbox (MITT) [33] was used for computing six segmental strain curves from the apical four-chamber view testing sequences filtered by the proposed 3D filter (trained with L_{rec}) and the 2D benchmark network. The latter network was considered to investigate whether independent filtering of the cluttered frames has an impact on the quality of the computed strain profiles. The segmental strain curves were also computed from the clutter-free sequences to serve as ground-truth, and from the cluttered sequences to see to which extent the clutter patterns disturb the speckle-tracking algorithm.

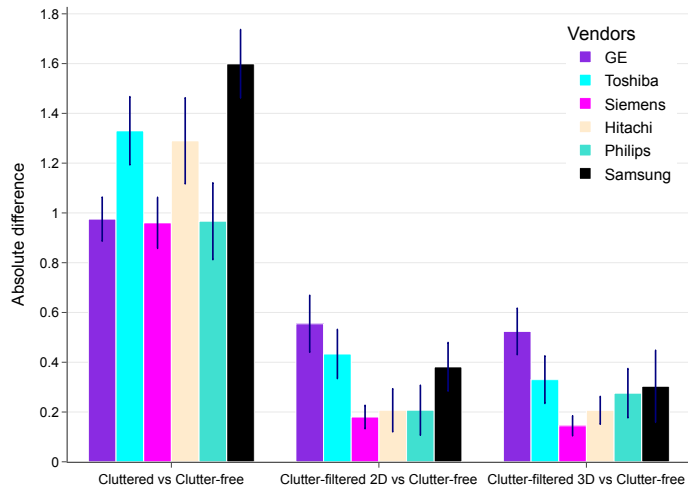


Figure 12: Absolute differences (Mean \pm STD) between the segmental strain curves computed from the cluttered and clutter-free sequences as well as clutter-filtered and clutter-free sequences. The filtered sequences of the proposed 3D network and its 2D counterpart, both trained using L_{rec} , were considered. The absolute differences were computed separately for each of the six vendors.

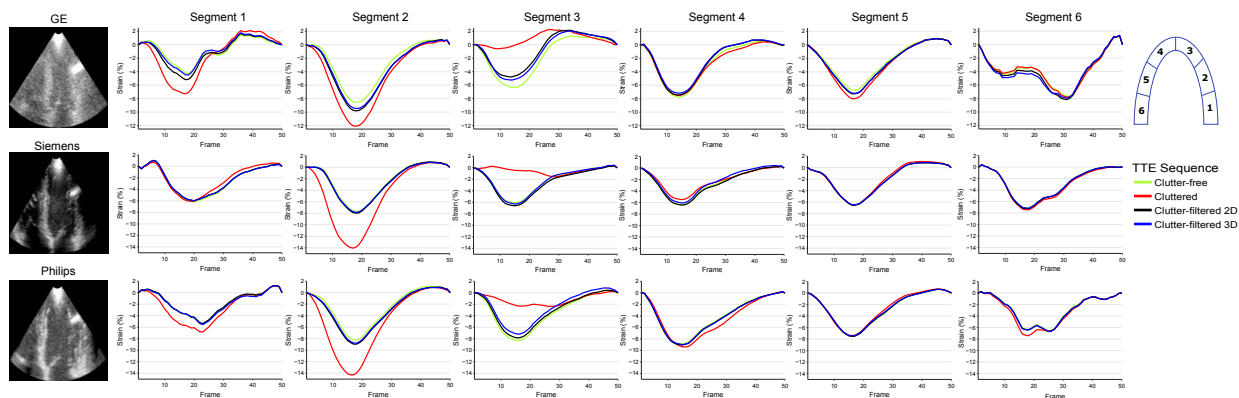


Figure 13: Examples of the segmental strain curves computed from the clutter-free, cluttered and clutter-filtered sequences of three vendors. The filtered sequences of the proposed 3D network and its 2D counterpart, both trained using L_{rec} , were considered. Approximate locations of the six LV segments on the apical four-chamber view are shown on the right-most columns

The cluttered sequences with a subset of the NF & RL patterns, as the most disturbing clutter patterns, were used for the strain analysis. Mean absolute differences (MADs) between the segmental strain curves of the clutter-free and clutter-filtered sequences are shown in Figure 12 for the 2D and 3D filters and the six vendors in the dataset. MADs between the segmental strain curves of the cluttered and clutter-free sequences are also shown in this figure. For all vendors, the MADs between the clutter-filtered and clutter-free strain curves are significantly smaller than those of the cluttered and clutter-free strain curves. This is the result of efficient filtering of the clutter patterns by the deep networks. Indeed for most of the vendors, the differences between the strain curves computed from the clutter-filtered and clutter-free sequences are very small implying that the image features of the clutter-filtered and clutter-free frames are very similar to each other. Another important observation that can be made is that for all but one of the vendors, the strain curves computed from the sequences filtered by the 3D network are more similar to those computed from the clutter-free sequences as compared to the 2D network, i.e. 3D MADs < 2D MADs. This is in line with the results obtained based on the coherence analysis in Section 4.3 and reconfirms the efficacy of the proposed 3D network for spatiotemporal clutter filtering of the TTE sequences.

For the NF & RL clutter pattern shown in Figure 8 and three of the vendors with large, small and medium MADs between the clutter-filtered and clutter-free sequences (see Figure 12), the computed segmental strain curves are illustrated in Figure 13. The left-most column of this figure shows the positions of the clutter patterns on the myocardial

wall to help associating the strain profiles with the cluttered and clutter-free segments. The RL clutter pattern was chosen to be moving to disturb the speckle-tracking algorithm throughout the cardiac cycle. Figure 13 shows that for the segments that are partially or fully contaminated by the clutter patterns, i.e. segments 1 to 4, the strain profiles computed from the cluttered sequences (red curves) are considerably different from those computed from the same segments of the clutter-free sequences (green curves). This confirms the negative impact of the artifact patterns on the performance of the speckle-tracking algorithm. For these segments, the strain curves computed from the clutter-filtered sequences are comparable to the clutter-free strain curves demonstrating the capability of the deep filtering networks in suppressing the clutter patterns and reconstructing the cluttered zones. Given that segments 5 and 6 - left-hand side on the shown frames - are almost free of artifacts, their strain profiles computed from the clutter-free, cluttered and clutter-filtered sequences are quite similar. This suggests that the filtering networks did not alter the image properties of the artifact-free zones which was one of the main aspects that was considered when designing the proposed model (see Section 2.3).

4.5 In-vivo analysis

All the results presented so far in this section were obtained using the synthetic TTE sequences and the simulated artifact patterns. Since the goal of designing the proposed clutter filtering network is to use it in clinical practice to enhance the quality of the acquired TTE sequences, it is important to evaluate the generalization performance of the proposed filtering network when dealing with real-world artifactual sequences. As such, the proposed 3D network that was trained using the synthetic TTE sequences and L_{rec} , was tested using an unseen in-vivo dataset containing 9 clinical recordings using a GE system that showed clear NR and/or RL clutter patterns. The trained 2D benchmark network was also tested using the in-vivo sequences to see if the 3D network can outperform its 2D counterpart on the real-world data as well.

Unlike the artifactual synthetic sequences, no ground-truth dataset was available for the in-vivo sequences. Therefore, it was not possible to compute MARE values for the filtered sequences. The following approaches were thus considered to evaluate the performance of the filtering networks: i) visual inspection of the filtered results, ii) coherence analysis.

For the first evaluation approach, the generated filtering results of a subset of the subjects, the middle frames, are shown in Figure 14. Absolute differences between the cluttered and clutter-filtered frames were also computed and are shown below the filtered frames. On the absolute difference images, the bright and dark regions mainly correspond to the cluttered and clutter-free zones on the artifactual images, respectively. This indicates that the deep filtering networks which were trained using the simulated artifact patterns only, could identify and suppress similar patterns on the in-vivo cluttered zones and did not change the characteristics of the clutter-free zones. The cine-loops of the sequences filtered by the 3D network, however, looked more spatiotemporally coherent than the sequences filtered by the 2D network. Video files of the filtered in-vivo sequences are provided in the Supplemental Material and the GitHub repository.

For the second evaluation approach, Z in Eq. 7 was computed using the absolute difference images shown in Figure 14. The incoherence score C (see Eq. 8) can be interpreted in the same way as for the synthetic data. A small C means that the variations of the pixel values of the cluttered zones on the consecutive filtered frames are negligible. The mean incoherence score of the proposed 3D filtering network was significantly smaller than that of the 2D network, 2.7 ± 1.7 vs 4.6 ± 1.7 ($p < 0.05$).

5 Conclusions

In this study, a deep spatiotemporal filtering network was proposed for removing different types of the reverberation clutters from the TTE sequences. To generate clutter-filtered sequences which are coherent both in space and time, the filtering network was designed using 3D convolutional layers and was built based on the U-Net model. The 3D U-Net was combined with the AG modules to highlight the clutter zones on the learned feature maps as the salient regions in order to aid the network removing the artifact patterns. To preserve fine structures of the clutter-free zones in the input images, the filtering network was trained based on residual learning.

A key requirement for training an efficient deep filtering network which has a good generalization performance and is able to remove different types of the clutter patterns from the images of the different ultrasound vendors, is having access to a big dataset of artifactual TTE sequences and their corresponding artifact-free sequences. Given that in the clinical practice such a dataset is not readily available, one of the main goals of the present study was to show the feasibility of training an efficient filtering network using realistic synthetic TTE sequences and simulated artifact patterns. The obtained experimental results confirmed the efficacy of the deep filtering network in terms of the generalization performance and suitability of the filtered frames for further processing.

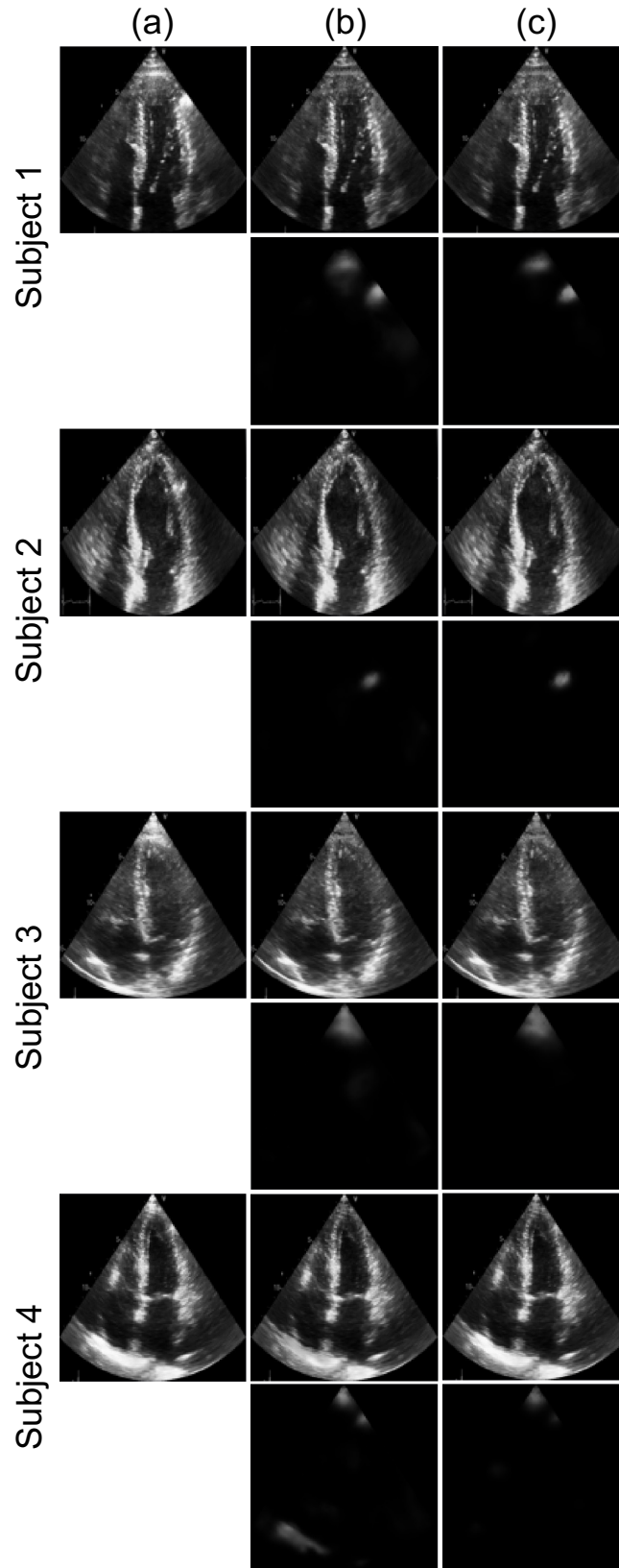


Figure 14: (a) Examples of the in-vivo frames of four different subjects which are contaminated by the NF and/or RL clutter patterns. (b) The frames filtered using the proposed 3D filtering network and (c) the 2D filtering network. Absolute differences between the cluttered and clutter-filtered frames are shown below the filtered frames.

Acknowledgments

We would like to thank Prof. Jens-Uwe Voigt, Department of Cardiovascular Sciences, KU Leuven, for providing us with the in-vivo dataset and Dr Lamia Al Saikhan, University College London, Institute of Cardiovascular Science, for helpful discussions and suggestions. The resources and services used in this work were provided by the VSC (Flemish Supercomputer Center), funded by the Research Foundation - Flanders (FWO) and the Flemish Government. The authors also acknowledge the financial support provided by National funds, through the Foundation for Science and Technology (FCT, Portugal), through project PTDC/EMD-EMD/1140/2020 and grant CEECIND/03064/2018 (S.Q.).

Data availability

The artifactual and artifact-free images used in this study can be obtained from the authors upon request.

References

- [1] Steinar Bjaerum, Hans Torp, and Kjell Kristoffersen. Clutter filter design for ultrasound color flow imaging. *IEEE Trans. Ultrason., Ferroelectr., Freq. Control*, 49(2):204–216, 2002.
- [2] Peter C Tay, Scott T Acton, and John A Hossack. A wavelet thresholding method to reduce ultrasound artifacts. *Computerized Medical Imaging and Graphics*, 35(1):42–50, 2011.
- [3] CH Alfred and Lasse Lovstakken. Eigen-based clutter filter design for ultrasound color flow imaging: A review. *IEEE Trans. Ultrason., Ferroelectr., Freq. Control*, 57(5):1096–1111, 2010.
- [4] F William Mauldin, Dan Lin, and John A Hossack. The singular value filter: A general filter design strategy for pca-based signal separation in medical ultrasound imaging. *IEEE Trans. Med. Imag.*, 30(11):1951–1964, 2011.
- [5] Javier S Turek, Michael Elad, and Irad Yavneh. Sparse signal separation with an off-line learned dictionary for clutter reduction in echocardiography. In *IEEE Convention of Electrical & Electronics Engineers*, pages 1–5, 2014.
- [6] Javier S Turek, Michael Elad, and Irad Yavneh. Clutter mitigation in echocardiography using sparse signal separation. *Journal of Biomedical Imaging*, pages 1–18, 2015.
- [7] Deepak Mishra, Santanu Chaudhury, Mukul Sarkar, and Arvinder Singh Soin. Ultrasound image enhancement using structure oriented adversarial network. *IEEE Signal Processing Letters*, 25(9):1349–1353, 2018.
- [8] Fabian Dietrichson, Erik Smistad, Andreas Ostvik, and Lasse Lovstakken. Ultrasound speckle reduction using generative adversarial networks. In *IEEE Int. Ultrason. Symp. (IUS)*, pages 1–4, 2018.
- [9] Ouwen Huang, Will Long, Nick Bottenus, Marcelo Lerenegui, Gregg E Trahey, Sina Farsiu, and Mark L Palmeri. Mimicknet, mimicking clinical image post-processing under black-box constraints. *IEEE transactions on medical imaging*, 39(6):2277–2286, 2020.
- [10] Dimitris Perdios, Manuel Vonlanthen, Adrien Besson, Florian Martinez, Marcel Arditi, and Jean-Philippe Thiran. Deep convolutional neural network for ultrasound image enhancement. In *IEEE Int. Ultrason. Symp. (IUS)*, pages 1–4, 2018.
- [11] Leandra L Brickson, Dongwoon Hyun, and Jeremy J Dahl. Reverberation noise suppression in the aperture domain using 3d fully convolutional neural networks. In *IEEE Int. Ultrason. Symp. (IUS)*, pages 1–4, 2018.
- [12] Gerhard-Paul Diller, Astrid E Lammers, Sonya Babu-Narayan, Wei Li, Robert M Radke, Helmut Baumgartner, Michael A Gatzoulis, and Stefan Orwat. Denoising and artefact removal for transthoracic echocardiographic imaging in congenital heart disease: utility of diagnosis specific deep learning algorithms. *The international journal of cardiovascular imaging*, 35(12):2189–2196, 2019.
- [13] Mahdi Tabassian, XingRan Hu, Bidisha Chakraborty, and Jan D’hooge. Clutter filtering using a 3d deep convolutional neural network. In *IEEE Int. Ultrason. Symp. (IUS)*, pages 2114–2117, 2019.
- [14] Tollef Struksnes Jahren, Anders Rasmus Sørnes, Bastien Dénarié, Erik Steen, Tore Bjåstad, and Anne H Schistad Solberg. Reverberation suppression in echocardiography using a causal convolutional neural network. *IEEE Access*, 2023.
- [15] Martino Alessandrini, Bidisha Chakraborty, Brecht Heyde, Olivier Bernard, Mathieu De Craene, Maxime Sermesant, and Jan D’hooge. Realistic vendor-specific synthetic ultrasound data for quality assurance of 2-d speckle tracking echocardiography: Simulation pipeline and open access database. *IEEE Trans. Ultrason., Ferroelectr., Freq. Control*, 65(3):411–422, 2017.

- [16] Ali Fatemi, Erik Andreas Rye Berg, and Alfonso Rodriguez-Molares. Studying the origin of reverberation clutter in echocardiography: in vitro experiments and in vivo demonstrations. *Ultrasound in medicine & biology*, 45(7):1799–1813, 2019.
- [17] Ion Codreanu, Tammy J Pegg, Joseph B Selvanayagam, Matthew D Robson, Oliver J Rider, Constantin A Dasanu, Bernd A Jung, David P Taggart, Stephen J Golding, Kieran Clarke, et al. Normal values of regional and global myocardial wall motion in young and elderly individuals using navigator gated tissue phase mapping. *Age*, 36(1):231–241, 2014.
- [18] Olaf Ronneberger, Philipp Fischer, and Thomas Brox. U-net: Convolutional networks for biomedical image segmentation. In *International Conference on Medical image computing and computer-assisted intervention*, pages 234–241. Springer, 2015.
- [19] Özgün Çiçek, Ahmed Abdulkadir, Soeren S Lienkamp, Thomas Brox, and Olaf Ronneberger. 3d u-net: learning dense volumetric segmentation from sparse annotation. In *Int. Conf. on Medical Image Comp. and Computer-assisted Interv.*, pages 424–432. Springer, 2016.
- [20] Kyong Hwan Jin, Michael T McCann, Emmanuel Froustey, and Michael Unser. Deep convolutional neural network for inverse problems in imaging. *IEEE Transactions on Image Processing*, 26(9):4509–4522, 2017.
- [21] Ding Liu, Bihan Wen, Jianbo Jiao, Xianming Liu, Zhangyang Wang, and Thomas S Huang. Connecting image denoising and high-level vision tasks via deep learning. *IEEE Transactions on Image Processing*, 29:3695–3706, 2020.
- [22] Kaiming He, Xiangyu Zhang, Shaoqing Ren, and Jian Sun. Deep residual learning for image recognition. In *Proceedings of the IEEE conference on computer vision and pattern recognition*, pages 770–778, 2016.
- [23] Saumya Jetley, Nicholas A Lord, Namhoon Lee, and Philip HS Torr. Learn to pay attention. In *International Conference on Learning Representations*, 2018.
- [24] Jo Schlemper, Ozan Oktay, Michiel Schaap, Mattias Heinrich, Bernhard Kainz, Ben Glocker, and Daniel Rueckert. Attention gated networks: Learning to leverage salient regions in medical images. *Medical image analysis*, 53:197–207, 2019.
- [25] Dzmitry Bahdanau, Kyunghyun Cho, and Yoshua Bengio. Neural machine translation by jointly learning to align and translate. *arXiv preprint arXiv:1409.0473*, 2014.
- [26] Deepak Pathak, Philipp Krahenbuhl, Jeff Donahue, Trevor Darrell, and Alexei A Efros. Context encoders: Feature learning by inpainting. In *Proceedings of the IEEE conference on computer vision and pattern recognition*, pages 2536–2544, 2016.
- [27] William Lotter, Gabriel Kreiman, and David Cox. Unsupervised learning of visual structure using predictive generative networks. *arXiv preprint arXiv:1511.06380*, 2015.
- [28] Ian Goodfellow. Nips 2016 tutorial: Generative adversarial networks. *arXiv preprint arXiv:1701.00160*, 2016.
- [29] Satoshi Iizuka, Edgar Simo-Serra, and Hiroshi Ishikawa. Globally and locally consistent image completion. *ACM Transactions on Graphics (ToG)*, 36(4):1–14, 2017.
- [30] Ian Goodfellow, Jean Pouget-Abadie, Mehdi Mirza, Bing Xu, David Warde-Farley, Sherjil Ozair, Aaron Courville, and Yoshua Bengio. Generative adversarial nets. *Advances in neural information processing systems*, 27, 2014.
- [31] Justin Johnson, Alexandre Alahi, and Li Fei-Fei. Perceptual losses for real-time style transfer and super-resolution. In *European conference on computer vision*, pages 694–711. Springer, 2016.
- [32] Naveen Kodali, Jacob Abernethy, James Hays, and Zsolt Kira. On convergence and stability of gans. *arXiv preprint arXiv:1705.07215*, 2017.
- [33] Sandro Queirós, Pedro Morais, Daniel Barbosa, Jaime C Fonseca, João L Vilaça, and Jan D’hooge. Mitt: medical image tracking toolbox. *IEEE transactions on medical imaging*, 37(11):2547–2557, 2018.